

## Optimized structure and electronic band gap of monolayer GeSe from quantum Monte Carlo methods

Hyeondeok Shin 

*Computational Science Division, Argonne National Laboratory, Argonne, Illinois 60439, USA*

Jaron T. Krogel 

*Material Science and Technology Division, Oak Ridge National Laboratory, Oak Ridge, Tennessee 37831-6494, USA*

Kevin Gasperich 


*Leadership Computing Facility, Argonne National Laboratory, Argonne, Illinois 60439, USA*

Paul R. C. Kent 

*Computational Sciences and Engineering Division and Center for Nanophase Materials Sciences Division, Oak Ridge National Laboratory, Oak Ridge, Tennessee 37831-6494, USA*

Anouar Benali 

*Computational Science Division, Argonne National Laboratory, Argonne, Illinois 60439, USA*

Olle Heinonen \*

*Material Science Division, Argonne National Laboratory, Argonne, Illinois 60439, USA*



(Received 10 November 2020; accepted 22 January 2021; published 10 February 2021)

We have used highly accurate quantum Monte Carlo methods to determine the chemical structure and electronic band gaps of monolayer GeSe. Two-dimensional (2D) monolayer GeSe has received a great deal of attention due to its unique thermoelectric, electronic, and optoelectronic properties with a wide range of potential applications. Density functional theory (DFT) methods have usually been applied to obtain optical and structural properties of bulk and 2D GeSe. For the monolayer, DFT typically yields a larger band-gap energy than for bulk GeSe but cannot conclusively determine if the monolayer has a direct or indirect gap. Moreover, the DFT-optimized lattice parameters and atomic coordinates for monolayer GeSe depend strongly on the choice of approximation for the exchange-correlation functional, which makes the ideal structure—and its electronic properties—unclear. In order to obtain accurate lattice parameters and atomic coordinates for the monolayer, we use a surrogate Hessian-based parallel line search within diffusion Monte Carlo to fully optimize the GeSe monolayer structure. The DMC-optimized structure is different from those obtained using DFT, as are calculated band gaps. The potential energy surface has a shallow minimum at the optimal structure. This, combined with the sensitivity of the electronic structure to strain, suggests that the optical properties of monolayer GeSe are highly tunable by strain.

DOI: [10.1103/PhysRevMaterials.5.024002](https://doi.org/10.1103/PhysRevMaterials.5.024002)

### I. INTRODUCTION

Group-IV monochalcogenides  $MX$  ( $M = \text{Ge}$  or  $\text{Sn}$ ,  $X = \text{S}$  or  $\text{Se}$ ) have received a great deal of attention because of their unique thermoelectric and electronic properties, which can be exploited in wide range of applications such as photodetection, gas sensing, and as potential anode materials for lithium-ion batteries [1–3]. In particular, germanium selenide (GeSe) is a two-dimensional (2D) layered  $p$ -type semiconductor that has been extensively studied because of its optical properties; however, they are still not yet fully understood. In the past few decades, bulk GeSe has been shown to

have an indirect band gap at room temperature by various experimental and theoretical studies [4–10]. Experimental results have provided indirect gap measurements in a range of 1.07–1.29 eV using different experimental methods, such as electron-energy-loss spectroscopy [11], diffuse reflectance spectroscopy [7], and ultraviolet photoemission spectroscopy [12]. Very recently, adsorption spectra measurements suggested the possibility of a direct band-gap minimum of 1.3 eV [13]. This spread in experimental results indicates a high sensitivity of measured GeSe optical properties to the particular choice of optical spectroscopy method used. Theoretical results on GeSe optical gaps have also shown to be strongly dependent on the relaxed GeSe structure as well as on the particular theoretical methodology used in the calculations. Several density functional theory (DFT) studies have been

\*heinonen@anl.gov

performed to investigate the optical properties of GeSe; however, the computed band gaps vary strongly with the particular exchange-correlation (XC) potential used in DFT Kohn-Sham Hamiltonian. For example, the generalized gradient approximation (GGA) is a well-known XC functional that has been widely applied to study structural and optical characteristics of various electronic structures. Many GGA optical gaps for bulk GeSe have been evaluated so far; however, as is typical, GGA tends to underestimate optical gaps compared to experiment [14]. Moreover, even within the same class of XC functional, different approximate DFTs have yielded significantly different optimized lattice parameters for the orthorhombic  $Pnma$  GeSe structure, with lattice parameters in the ranges of  $a = 4.21 \text{ \AA}$  to  $4.83 \text{ \AA}$ ,  $b = 3.78 \text{ \AA}$  to  $3.86 \text{ \AA}$ , and  $c = 10.60 \text{ \AA}$  to  $14.69 \text{ \AA}$  [14,15]. This points to an intrinsic limitation of DFT approximations when applied to optical and structural properties for GeSe and motivated us to use a highly accurate numerical approach which allows for full incorporation of electron correlation and interlayer interaction for layered GeSe.

Detailed experimentally determined structural and optical properties of monolayer GeSe have not yet been reported, so these properties have largely been obtained using first-principle calculations. According to previous DFT studies, monolayer GeSe is expected to be a direct-gap semiconductor with a larger band gap than bulk GeSe, and its gap can be tuned using uniaxial or biaxial strains [14]. This strain sensitivity of the optical properties of monolayer GeSe clearly shows the importance of obtaining an accurate monolayer chemical structure in order to accurately predict its band-gap energy. Strain could be applied either directly or via a substrate or heterostructure. The DFT-optimized monolayer chemical structure exhibits a distorted NaCl-type structure, but the exact structural parameters for the distortion, as well as the equilibrium lattice parameters, are not known for the monolayer: DFT-GGA calculations have yielded monolayer relaxed lattice parameters of  $a = 3.99\text{--}4.83 \text{ \AA}$  and  $b = 3.78\text{--}3.97 \text{ \AA}$  [14,16,17]. This huge variation makes it difficult to ascertain the monolayer chemical structure and also difficult to assess the accuracy of reported DFT band gaps of  $0.8\text{--}1.8 \text{ eV}$  [14,15], because these values from separate DFT studies were usually obtained from different structural parameters for the monolayer. Consequently, this range of DFT results leads us to conclude that an accurate benchmark calculation of the geometry of pristine monolayer GeSe is needed in order to accurately estimate optical properties and their qualitative and quantitative changes induced by strains.

Quantum Monte Carlo (QMC) is a highly accurate class of stochastic method which can describe the ground-state properties of many-body electronic structures. Previous QMC studies have successfully provided accurate structural properties for various functional materials, including 2D layered systems [18–21]. In this study we used QMC to study structural and optical properties of bulk and monolayer GeSe. More recently, Wines *et al.* [22] used QMC methods to obtain the lattice constants and band gaps of monolayer GaSe. Our results are analogous to theirs in that Wines *et al.* showed that there is a large spread in DFT results for structure and band gaps, and they also showed that many-body perturbation theories such as the Bethe-Salpeter equation also underesti-

mate band gaps compared to results using diffusion Monte Carlo (DMC). In order to describe accurate distortions in the NaCl-type monolayer structure, we fully optimized the GeSe monolayer geometry using QMC. Finally, we used DMC to estimate optical gaps of the optimized monolayer geometry and observed significantly larger band-gap energies than either DFT band gaps for monolayer GeSe or experimental values for bulk GeSe. We also verified using multideterminant expansions of the ground state and excited states that the fixed-node approximation from single-determinant trial wave functions did not introduce any appreciable errors in the estimated DMC band gaps.

## II. COMPUTATIONAL DETAILS

Our QMC calculations were carried out with the fixed-node DMC method [23,24] as implemented in the QMCPACK code [25,26]. Slater-Jastrow type wave functions were used as trial wave functions, consisting of a single Slater determinant and Jastrow correlation functions with up to three-body correlations. Single-particle orbitals in the Slater determinants were obtained with the DFT Kohn-Sham scheme based on plane-wave basis sets using the QUANTUM EXPRESSO package [27]. The Perdew-Burke-Ernzerhof (PBE) parametrization [28] of GGA was employed as the XC functional, and the plane-wave calculations used a 350 Ry (about 4,762 eV) kinetic energy cutoff for the energy-consistent norm-conserving Ge and Se pseudopotentials developed by Burkatzki, Fillip, and Dolg (BFD) [29,30]. We used the same pseudopotentials for all DFT and QMC calculations, except for the multideterminant expansions (below). Bulk and monolayer GeSe were simulated with Monkhorst-Pack  $8 \times 8 \times 8$  (bulk) and  $8 \times 8 \times 1$  (monolayer)  $k$ -point grids; a 20- $\text{\AA}$ -thick vacuum padding was added along the  $z$  axis (perpendicular to the plane of the monolayer) for the monolayer. All DMC calculations in this study were done with a  $0.005 \text{ Ha}^{-1}$  time step, which was shown to be a fully converged value in previous DMC studies of various periodic 2D systems [18,20]. The one-body finite-size effects from the periodic supercell DMC calculations were fully controlled by applying twist-averaged boundary conditions (TABC) [31]. (See Appendix A for details on convergence with respect to the  $k$ -point grid and TABC.) We additionally reduced the two-body finite-size effect by extrapolating DMC energies estimated at various supercell sizes to the bulk limit.

In addition, we performed in this study selected configuration-interaction (sCI) calculations using the configuration interaction using a perturbative selection made iteratively (CIPSI) method [32] in order to compare the band-gap energy computed with the CIPSI multideterminant wave function to the single-determinant DMC band-gap energy. All CIPSI calculations in this study were performed with a modified version of Quantum Package 2 [33] using integrals from PySCF [34] and used correlation-consistent effective core potentials (ccECPs) with the double-zeta (DZ) and triple-zeta (TZ) basis sets developed for use with these ccECPs [35]. Each multistate CIPSI calculation was performed using matching to the renormalized second-order perturbative correction to the energy [33]. For each DZ and TZ basis, an initial two-state CIPSI calculation was performed using DFT orbitals

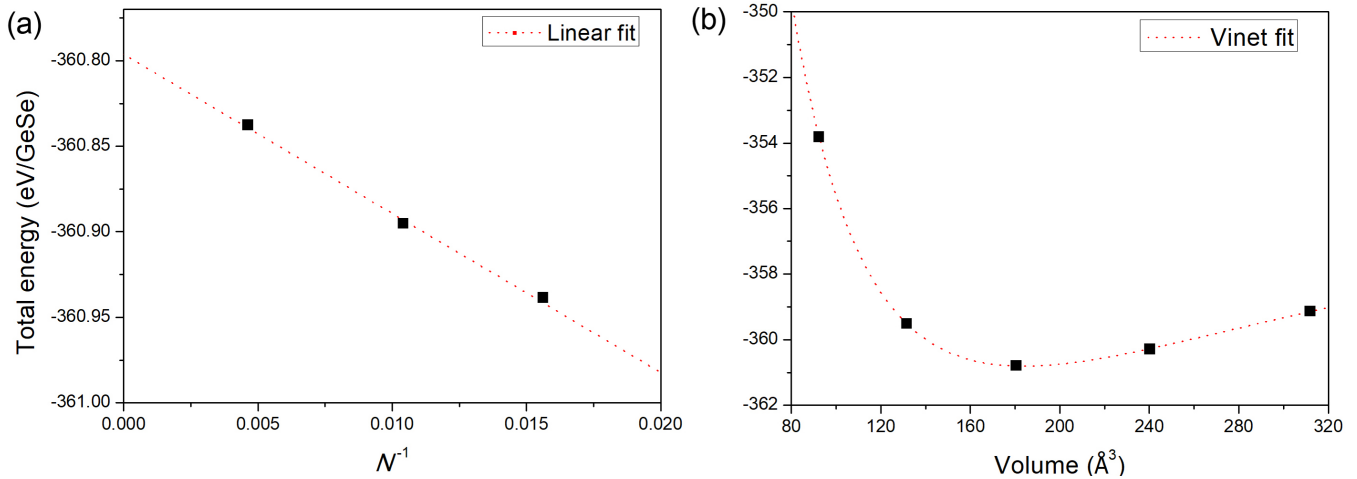


FIG. 1. (a) DMC total energy of bulk GeSe as function of  $N^{-1}$ , where  $N$  is the total number of atoms in the supercell. The dotted line indicates a simple linear regression fit. (b) Extrapolated DMC total energy of GeSe as function of unit-cell volume. The dotted line represents a Vinet fit.

obtained with the B3LYP XC functional [36–39] until the size of the variational space reached  $10^5$  determinants. Natural orbitals (NOs) were formed from the resulting multideterminant wave functions (with equal weights for each state), and a second two-state CIPSI calculation was performed in the space of these NOs with a larger number of determinants (about  $9 \times 10^6$ ). For the calculations in the TZ basis, this process of forming NOs was repeated after reaching  $10^6$  determinants within the first set of NOs, and then a second two-state CISPI calculation with about  $10^7$  determinants. Estimated full-CI energies were obtained via linear extrapolation of the CIPSI variational energies with respect to the renormalized second-order perturbative correction to the energy (rPT2) as  $\text{rPT2} \rightarrow 0$ .

### III. RESULTS

We first computed the equation of state for bulk GeSe using fixed-node (FN) DMC in order to assess the structural and optical properties of bulk GeSe and to verify the DMC results against available experimental values. Figure 1(a) shows the DMC total energies for bulk GeSe with respect to the inverse of the number of atoms  $N$  per supercell at the experimental lattice parameters  $a = 4.38$ ,  $b = 3.82$ , and  $c = 10.79$  Å [40]. Three different sizes of supercell with up to 108 formula units (f.u.) of GeSe were simulated using TABCs with up to 64 twists in order to minimize the one-body finite-size effect. Figure 1(a) shows that linear regression provided an excellent fit for TABC-DMC total energies in the thermodynamic limit, and the extrapolated total energy was estimated to be  $-360.796(3)$  eV/f.u. Using the same protocol, we calculated extrapolated TABC-DMC total energies at various unit-cell volumes in order to obtain the equation of state. We calculated the DMC energy by changing the unit-cell volume, keeping the aspect ratio and (relative) atomic coordinates fixed. Using the Vinet function to fit the equation of state, as shown in Fig. 1(b), the equilibrium DMC lattice parameter  $a$  and bulk modulus were estimated as  $4.40(1)$  Å and  $32.1(3)$  GPa, respectively, which are in good agreement with the experimental

values of  $4.40$  Å and  $37.9$  GPa. The DMC cohesive energy for bulk GeSe was calculated as  $6.91(2)$  eV/f.u. As the experimental cohesive energy for bulk GeSe is not reported yet to the best of our knowledge, we expect that this DMC cohesive energy can give good guidance to assess the energetic stability of GeSe-based materials, as DMC has been shown to yield accurate cohesive energies in many materials [18,41–44].

We then carried out DMC calculations to estimate the band gaps of bulk GeSe. DMC excitonic gaps can be evaluated by computing  $E_g^{ex} = E_{ph}(\mathbf{k}) - E_0$ , where  $E_0$  and  $E_{ph}(\mathbf{k})$  represent the ground-state energy and the DMC total energy upon a particle-hole excitation, particle-hole excitation energy, respectively, with the latter estimated by promoting an electron from the top of the valence band to the bottom of the conduction band at a momentum  $\mathbf{k}$ . In order to find the relevant single-particle momentum  $\mathbf{k}$ , we plotted the DFT band structure for bulk GeSe using DFT-PBE. In the PBE band structure of bulk GeSe [see Fig. 2(a)], we can see that the direct minimum gap minimum is located at the high-symmetry  $\Gamma$  point, which is the  $\mathbf{k}$  point at which we calculated the excitonic gap. We verified that the band structure obtained using PBE0 gave the same direct and indirect gaps as the PBE band structure (see Appendix C for details). In addition to the excitonic gap, we also estimated the DMC quasiparticle gap by calculating the ground-state total energy difference of  $N + 1$ ,  $N - 1$ , and  $N$  electron systems,  $E_g^{qp} = E(N + 1) + E(N - 1) - 2E(N)$ . Both the DMC excitonic and the quasiparticle gaps were fully extrapolated to the bulk thermodynamic limit using a simple linear regression fit, with estimated DMC gaps in different supercell sizes of 32, 72, and 108 f.u. supercells, as can be seen in Fig. 2(b). The extrapolated excitonic direct gap was calculated to be  $1.62(16)$  eV, which is in good agreement with the experimental result for the direct gap,  $1.53$  eV [45]. The extrapolated quasiparticle gap of  $1.95(21)$  eV is seemingly larger than the excitonic gap, although the two values are within each others' error bars. In any case, one would expect the excitonic gap to be smaller by an amount equal to the exciton binding energy; our results suggest a weak exciton binding energy  $\sim 0.3$  eV.

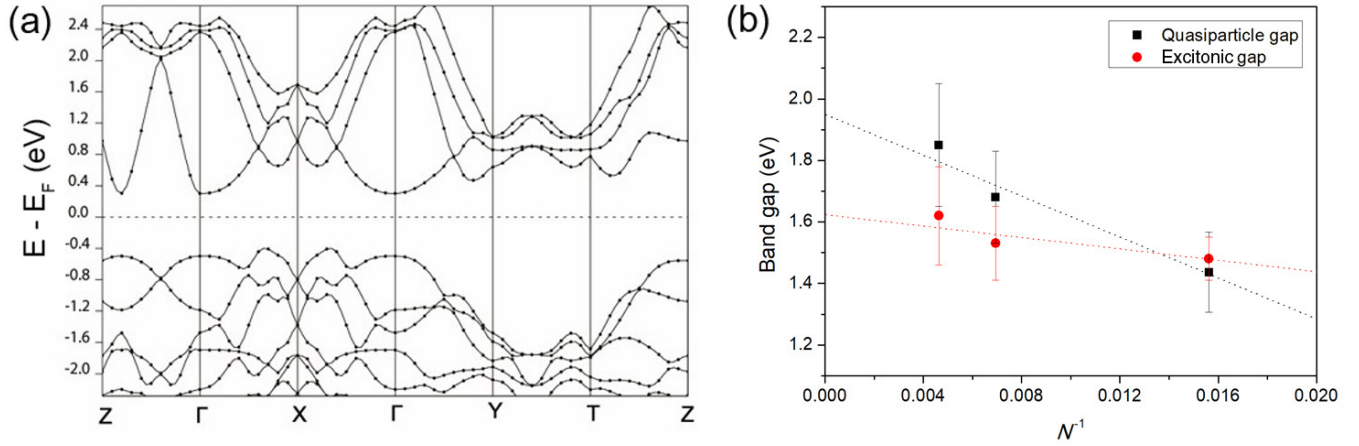


FIG. 2. (a) PBE band structure of bulk GeSe. (b) DMC excitonic gap and quasiparticle gap for bulk GeSe as function of  $N^{-1}$ , where  $N$  is the total number of atoms in the supercell. The dotted line indicates a simple linear regression fit.

Computed direct-gap and structural properties of bulk GeSe in this study are summarized in Table I. Among the XC functionals in Table I, there is no single DFT XC functional that simultaneously yields structural properties and band gap, in reasonable agreement with experimental values. For example, the PBE0 lattice parameters and cohesive energy are in good agreement with the experimental or DMC values, but the PBE0 band gap is significantly larger than the experimental one. In contrast, the DMC results are in good agreement with the experimental results for both structural properties and band gap. Based on our accurate DMC results for bulk GeSe, we can confidently assume that DMC will enable us to predict accurate structural properties and band gap of monolayer GeSe, as well to guide future experiments and computational works.

We now turn to the monolayer form of GeSe. In order to study monolayer GeSe, it is necessary to obtain an accurate monolayer structure, which is not known yet experimentally. In experiments, the monolayer geometry will also be affected by the substrate used. That is an additional complication that

TABLE I. Equilibrium lattice constant ( $a$ ), bulk modulus ( $B_0$ ), cohesive energy ( $E_{\text{coh}}$ ), and band gap ( $E_g$ ) for bulk GeSe computed using various DFT XC functionals and DMC;  $E_g^{\text{ex}}$  and  $E_g^{\text{qp}}$  are the excitonic and quasiparticle gap, respectively.

Method	$a$ (Å)	$B_0$ (GPa)	$E_{\text{coh}}$ (eV)	$E_g$ (eV)
PBE	4.43	28.9	6.89	0.68
LDA	4.38	32.8	8.54	0.58
SCAN	4.43	30.0	–	0.88
PBE0	4.38	33.2	6.96	1.88
B3LYP	4.48	27.1	6.06	1.77
HSE06	4.38	32.4	5.97	1.21
DMC	4.40(1)	32.1(3)	6.91(2)	$E_g^{\text{ex}} : 1.62(16)$ $E_g^{\text{qp}} : 1.95(21)$
Exp.	4.40 <sup>a</sup>	37.9 <sup>b</sup>	–	1.53 <sup>c</sup>

<sup>a</sup>Reference [40].

<sup>b</sup>Reference [46].

<sup>c</sup>Reference [45].

we will not consider here but will focus on the unstrained equilibrium structure of monolayer GeSe. As seen in Fig. 3, there are a total of eight structural parameters that need to be optimized for the monolayer geometry. Direct structural optimization based on force minimization is not yet fully developed in efficient algorithms in QMC methods, and a brute-force optimization by mapping out the energy landscape as a function of eight degrees of freedom would be prohibitively expensive. Direct structural optimization based on force minimization, while developed and implemented for variational Monte Carlo (VMC) by Sorella and Capriotti [47], and also by Moroni *et al.* [48], is not yet fully developed in efficient DMC algorithms, particularly for solids and heavier elements. In contrast, DFT is routinely used to optimize a given structure based on force minimization. Therefore, we first optimized the monolayer structure using DFT in order to get a rough estimate of its geometry and of the difference between monolayer and bulk structures.

Table II shows structural parameters for fully relaxed monolayer GeSe using various DFT XC functionals. When we compare the DFT results for monolayer to the experimental values for bulk GeSe, we see large differences in the GeSe structural parameters between monolayer DFT and experimental results. However, because of the strong variation of the calculated structural parameters for monolayer GeSe with the DFT XC functional, we cannot at this point assertively claim that the monolayer geometry is different from that of the bulk. In particular, the Strongly Constrained and Appropriately Normed (SCAN) meta-GGA shows a significantly larger lattice parameter  $a$  than is obtained from other XC functionals for monolayer or bulk GeSe. Based on the large variation within the DFT results, we conclude that structural optimization using DMC is necessary.

As stated earlier, force-minimization methods for QMC DMC are not well developed. We therefore used an energy-minimization method based on the DMC total energy and without use of DMC energy gradients. A total of eight structural parameters consisting of two lattice parameters and six atomic coordinates are not straightforward to fully optimize manually; if we were to use a quartic function, which has been widely used for geometry optimization [49,50], optimizing

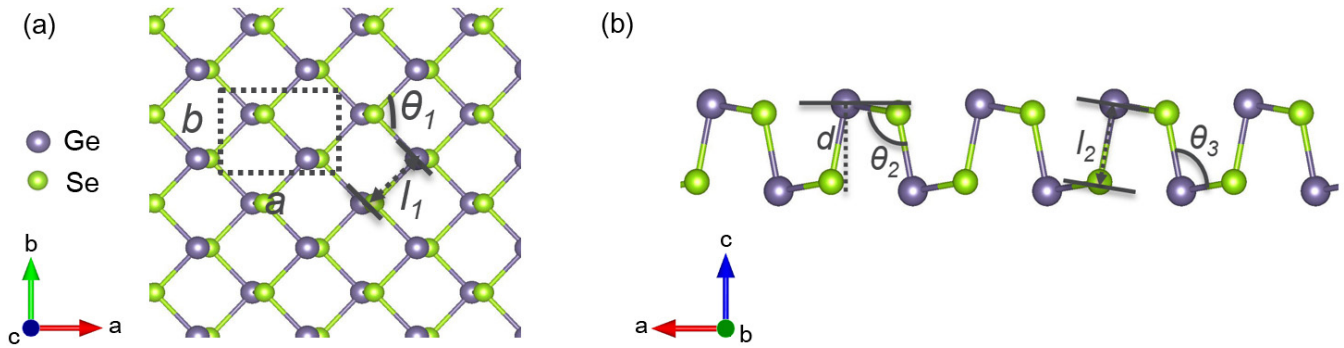


FIG. 3. (a) Top and (b) side view of GeSe monolayer. Parameters in the geometry are taken from Ref. [14].

the monolayer structure would require at least  $5^8$  grid points in order to estimate the global minimum in the energy surfaces for eight structural parameters. Because such a brute-force method requiring a total of 390 625 DMC total energy calculations would be prohibitively expensive, we introduce two distinct ways to efficiently optimize the monolayer structure using DMC with a reduced set of degrees of freedom.

#### A. DMC lattice parameter optimization with DFT atomic coordinates

We first computed a  $5^2$  DMC energy data grid for optimizing only the lattice parameters  $a$  and  $b$  for the monolayer, while the remaining internal atomic coordinates ( $d$ ,  $l_1$ ,  $l_2$ ,  $\theta_1$ , and  $\theta_2$ —see Fig. 3) were relaxed using DFT at a given pair of lattice parameters  $a$  and  $b$ . This replaces the six parameters for the internal atomic coordinates with the relaxed DFT results. Therefore, the choice of the DFT XC functional used to relax the atomic coordinates is very important in order to obtain the best possible DFT atomic coordinates. In order to choose a XC functional for the relaxation, we calculated DMC total energies at a few different lattice parameters and with DFT internal atomic coordinates relaxed (at fixed lattice parameters) using various XC functionals. In order to select the DFT XC functional for the relaxation of the internal atomic coordinates, we first did a screening of various DFT functionals. We fixed the lattice parameter  $b$  at 3.95 Å and selected four different values of the lattice parameter  $a$ . For each value of  $a$ , we then optimized the atomic coordinates using six different DFT XC functionals and finally calculated the DMC energy for the given lattice parameters  $a$  and  $b$  and the optimized atomic coordinates, in total, 24 DMC calculations. These cal-

culations suggested that the HSE06 XC functional provides the best atomic coordinates as the DMC total energy was lowest for the HSE06-optimized atomic coordinates. We then proceeded with the 25 DMC energy calculations scanning lattice parameters  $a$  and  $b$  for fixed (relative) atomic coordinates given by the HSE06 optimization. We will denote this DMC energy “DMC(HSE06).” Details of the DMC computations using relaxed DFT atomic coordinates can be found in Appendix B.

This optimization procedure yields an energy as a function of the lattice parameters  $a$  and  $b$ . As can be seen in the total energy contour plot in Fig. 4, the DMC(HSE06) energy minimum is located at  $a = 4.73(1)$  Å and  $b = 3.76(1)$  Å, which is far away from the PBE(HSE06) energy minimum (DFT-PBE total energy calculated with the HSE06-optimized atomic coordinates) of  $a = 4.26$  Å and  $b = 3.95$  Å. This significant difference between the DMC(HSE06) and PBE(HSE06) energy landscapes strongly suggests that the fully optimized DMC and DFT geometries are rather different. Moreover, PBE and HSE06 optimizations of the atomic coordinates yield very different results (Table II), while PBE and PBE(HSE06) optimizations of the lattice parameters yield almost identical results. This suggests that the DFT underestimates the difference in forces between the PBE and HSE06 atomic coordinates. Moreover, we found that the PBE(HSE06) optimized lattice parameters  $a$  and  $b$  are identical to the fully relaxed PBE lattice parameters even though their internal atomic coordinates are different (see Table II). This can be understood to originate in erroneously negligible differences between the PBE and HSE06 computed atomic forces, which leads us to suspect that the atomic force evolution is underestimated in the DFT relaxation process. On the other hand, we see a large discrepancy between the lattice parameters obtained from DMC(HSE06) and the fully relaxed HSE06 result, the latter with  $a = 4.38$  Å and  $b = 3.99$  Å, even though the same HSE06 functional was used in the relaxation of the atomic coordinates. This tells us that among the tested DFT XC functionals, HSE06 yields the best atomic coordinates, although they still differ discernibly from those obtained from DMC and still yield large errors in the lattice parameters. This tells us that among the DFT XC functionals, HSE06 yields relatively accurate optimized atomic coordinates but can still yield large errors in the lattice parameters. Thus we conclude that lattice parameters and atomic coordinates need to be optimized simultaneously using a fully DMC-based energy-minimization method.

TABLE II. Relaxed geometry of a GeSe monolayer using various DFT XC functionals. The experimental values are for bulk GeSe.

	$a$ (Å)	$b$ (Å)	$d$ (Å)	$l_1$ (Å)	$l_2$ (Å)	$\theta_1$ (deg)	$\theta_2$ (deg)	$\theta_3$ (deg)
PBE	4.26	3.95	2.50	2.65	2.52	96.5	93.9	97.2
LDA	4.03	3.96	2.51	2.71	2.51	93.9	89.3	96.0
SCAN	4.71	3.76	2.46	2.57	2.54	94.2	103.6	95.4
PBE0	4.21	3.85	2.48	2.58	2.51	96.5	100.3	91.8
B3LYP	4.47	3.89	2.51	2.56	2.51	96.9	98.5	96.7
HSE06	4.38	3.99	2.46	2.63	2.50	98.8	101.3	93.2
Exp. (Bulk) <sup>a</sup>	4.40	3.85	2.49	2.58	2.54	95.4	103.6	90.8

<sup>a</sup>Reference [45].

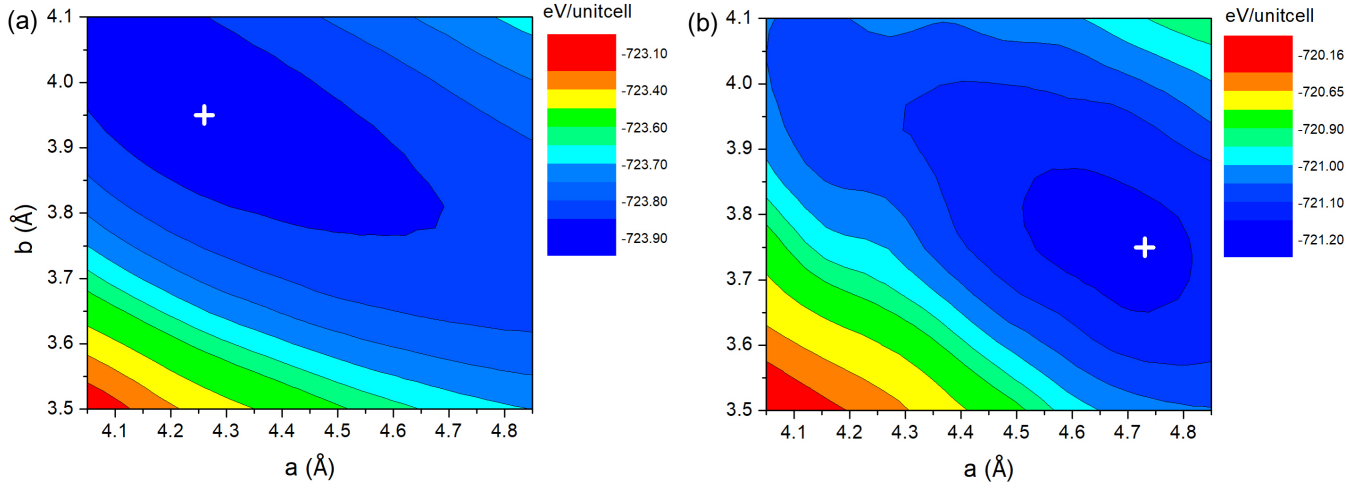


FIG. 4. Total energy contour plots for (a) PBE(HSE06) and (b) DMC(HSE06) energies as functions of lattice parameters  $a$  and  $b$  in atomic units. Crosses indicate global minima of the energy contours.

### B. DMC geometry optimization using a surrogate Hessian-based parallel line search method

As stated earlier, optimization of crystal structures with multiple cell and/or internal parameters is generally a challenge for DMC as forces and stresses are not yet widely available. Energy-based methods may instead be used; however, these generally require many costly energy evaluations in order to sample the atomic potential energy surface (PES) in sufficient detail to determine the optimal structure. Here, we briefly outline a surrogate Hessian-based optimization method that accelerates the search for the DMC PES optimum by incorporating approximate information from the DFT-energy Hessian. This significantly reduces the number of DMC calculations required. The full details of this method will be the subject of an upcoming publication.

The method combines line search with information from the DFT energy Hessian. The line search is a robust method to locate minima of multidimensional functions, and it is often used in QMC optimization methods for wave-function

parameters [25]. A potential drawback of line search is slow convergence, potentially requiring many iterations and hence many calculations of the DMC total energy. If the DMC energy Hessian were available, it could significantly accelerate the search. We instead guide the search using the approximate DFT Hessian, which still provides significant acceleration. For GeSe, the DFT energy Hessian was evaluated in the parametric subspace spanned by cell parameters  $a$ ,  $b$  and internal parameters  $x$ ,  $z_1$ ,  $z_2$ , where  $x$ ,  $z_1$ ,  $z_2$  are fractional coordinates of the four atoms in the unit cell, the positions of which are Ge( $x$ , 0.25,  $z_1$ ), Ge( $x + 0.5$ , 0.75,  $1 - z_1$ ), Se(0.5, 0.25,  $1 - z_2$ ), and Se(0, 0.75,  $z_2$ ), respectively. We noted that DFT-optimized structures would yield fixed atomic fractional coordinates  $y$  along the  $b$  axis for all XC functionals used. Therefore we could fix the atomic fractional coordinate  $y$  and use symmetry constraints for the remaining fractional coordinates to reduce the number of degrees of freedom to 3 for the internal atomic coordinate plus 2 for the lattice parameters. The explicit relations between  $(l_1, l_2, d, \theta_1, \theta_2, \theta_3)$  and  $(a, b, c, x, z_1, z_2)$  are

$$\begin{aligned}
 l_1^2 &= (xa)^2 + (0.5b)^2 + [(z_1 - z_2)c]^2 \\
 l_2^2 &= [(x - 0.5)a]^2 + \{[(z_1 + z_2) - 1]c\}^2 \\
 d &= [(z_1 + z_2) - 1]c \\
 \theta_1 &= 2 \tan^{-1} \left[ \frac{0.5b}{\sqrt{x^2a^2 + (z_1 - z_2)^2c^2}} \right] \\
 \theta_2 &= \cos^{-1} \left[ \frac{(2x - 1)xa^2 + 2(z_1 - z_2 - z_1^2 + z_2^2)c^2}{2\sqrt{(0.5 - x)^2a^2 + (1 - z_2 - z_1)^2c^2}\sqrt{x^2a^2 + 0.25b^2 + (z_1 - z_2)^2c^2}} \right] \\
 \theta_3 &= \cos^{-1} \left[ \frac{(2x - 1)xa^2 + 2(z_2 - z_1 - z_2^2 + z_1^2)c^2}{2\sqrt{(0.5 - x)^2a^2 + (1 - z_2 - z_1)^2c^2}\sqrt{x^2a^2 + 0.25b^2 + (z_1 - z_2)^2c^2}} \right], \tag{1}
 \end{aligned}$$

where  $c$  is the dimension of the simulation supercell along the  $z$  axis (coincident with the crystallographic  $c$  axis in Fig. 3) that includes vacuum padding. In our simulations,  $c = 21.58 \text{ \AA}$ .

The Hessian was found in this subspace by a quadratic fit to direct PBE energy values calculated on a uniform grid containing five points along each dimension. Next, the Hessian so obtained was diagonalized to yield a set of search directions

TABLE III. Progress of DMC energy and structural parameters for the GeSe monolayer during the parallel line search. Step 0 corresponds to the PBE relaxed geometry, which was the starting point of the search. Error bars corresponding to the 1- $\sigma$  uncertainty of the last significant digits are shown in parentheses for each quantity.

Step	$E_{\text{DMC}}$ (eV/unit cell)	$a$ (Å)	$b$ (Å)	$x$	$z_1$	$z_2$
0	-721.0684(49)	4.26	3.95	0.4140	0.55600	0.56000
1	-721.1277(98)	4.27(2)	3.95(1)	0.402(6)	0.5603(3)	0.5536(4)
2	-721.1432(38)	4.40(1)	3.89(1)	0.399(3)	0.5607(3)	0.5528(4)
3	-721.1533(38)	4.40(2)	3.89(1)	0.400(3)	0.5604(2)	0.5532(2)

within this parameter space. In this diagonalization step, we find that the lattice parameters  $a$  and  $b$  are coupled, parameters  $z_1$  and  $z_2$  are coupled, while  $x$  is essentially independent. If the DFT Hessian is a perfect surrogate for the DMC Hessian (i.e., no error) and if the energy surface is locally well approximated by a multidimensional quadratic function, then performing a line search along each of the separate directions in parallel converges to the DMC PES minimum in a single step.

In practice, for GeSe convergence was achieved by the second step. The search began from the PBE relaxed geometry. In each step, seven DMC calculations were performed along each parameter direction (31 calculations in total as all search directions shared a common point), and the energy curve along each line was approximated by a least-squares quartic polynomial fit. The minimum along each separate direction defined the starting parameter coordinate for the next iteration of the search. Table III contains the convergence of the structural parameters with search step. As the structural parameters converge, the total energy also converges to sub-millihartree accuracy.

Table IV summarizes the optimized DMC structural parameters for the GeSe monolayer. The DMC(HSE06) internal atomic coordinates are in general in better agreement with the DMC ones than are the PBE ones, but the differences in lattice parameters  $a$  and  $b$  are large; HSE06 does not simultaneously yield accurate atomic coordinates and lattice parameters. While the DMC(HSE06) internal atomic coordinates are in rather good agreement with the DMC ones, the differences in lattice parameters  $a$  and  $b$  are large, which clearly shows that HSE06 does not simultaneously yield accurate atomic coordinates and lattice parameters. In the DMC geometry optimization, the initial geometry was set to the relaxed PBE monolayer geometry, which has a smaller lattice parameter  $a$  and larger  $b$  than the experimental bulk lattice parameters, but the DMC relaxed geometry is close to the bulk GeSe one in terms of lattice parameters and the six atomic coordinates. We conclude that the absence of the interlayer interactions in the monolayer form does not give rise

to significant changes in the lattice parameters but does give rise to some differences in the internal atomic coordinates. Having obtained the optimized GeSe monolayer structure, we can calculate the interlayer binding energy of GeSe by computing the total energy difference between the bulk and monolayer forms. The interlayer binding energy extrapolated to the bulk limit is estimated to be 0.27(2) eV. Because the experimental binding energy is not yet reported, this DMC binding energy can serve an accurate guide for predicting interlayer binding energies for multilayer GeSe for future studies.

### C. Electronic band gaps

With the fully optimized DMC monolayer geometry, we examined carefully how the electronic band structure and band gaps in the DMC geometry differ from those of DFT geometries, which are the ones that have generally been used. In the PBE band structure (based on the PBE-relaxed geometry), the direct gap and indirect band gaps are located between  $X$  and  $Y$  high-symmetry points [see blue lines in Fig. 5(a)]. Among these two band gaps in the PBE band structure, it is difficult to confidently confirm the band-gap position because of the very small energy difference (about 0.05 eV) between the direct (1.06 eV) and indirect PBE gaps (1.01 eV). In Fig. 5(b), the PBE band structure based on the DMC geometry exhibits larger band gaps than the PBE geometry, but the minimum band gaps are located at the same  $k$  points as for the PBE geometry for both the direct (1.24 eV) and indirect gaps (1.02 eV). However, the direct gap is 1.50 eV at the  $\Gamma$  point in the DMC geometry, which is significantly smaller than the band gap (2.32 eV) in the PBE geometry. This clearly shows that the GeSe monolayer band structure is very sensitive to the precise structure. As a consequence, it is very important to accurately predict the structure in order to obtain accurate electronic structure. It also suggests that controlling strain, e.g., by using different substrates or by mechanical bending of samples, can be a route to manipulate the electronic properties of monolayer GeSe, in particular its optical absorption.

TABLE IV. Relaxed PBE and DMC geometry of the GeSe monolayer. The experimental values are for *bulk* GeSe geometry.

	$a$ (Å)	$b$ (Å)	$d$ (Å)	$l_1$ (Å)	$l_2$ (Å)	$\theta_1$ (deg)	$\theta_2$ (deg)	$\theta_3$ (deg)
PBE	4.26	3.95	2.50	2.65	2.52	96.5	93.9	97.2
DMC(HSE06)	4.73(1)	3.76(1)	2.44	2.56	2.53	94.2	103.1	96.4
DMC	4.40(2)	3.89(1)	2.45(1)	2.63(1)	2.49(1)	95.4(5)	100.2(2)	93.4(2)
Exp. (bulk) <sup>a</sup>	4.40	3.85	2.49	2.58	2.54	95.4	103.6	90.8

<sup>a</sup>Reference [45].

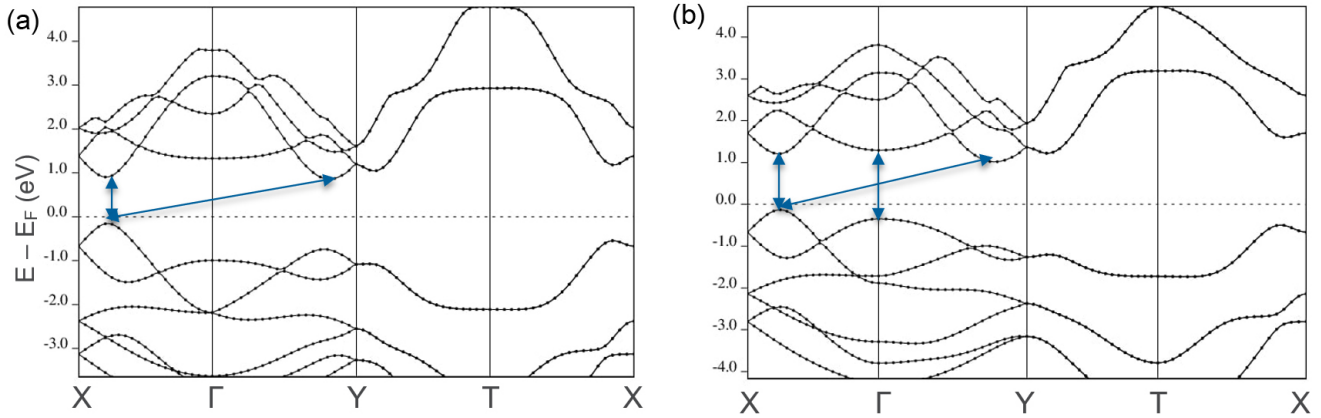


FIG. 5. PBE monolayer GeSe band structure for (a) PBE and (b) DMC geometry. Blue lines represent candidates for direct and indirect gap.

In order to obtain accurate band gaps, we estimated DMC gaps at selected  $\mathbf{k}$  points in the Brillouin zone, two direct and one indirect gap, based from the PBE band structure in the DMC geometry (see Fig. 5). Table V shows a summary of the results for the DFT and DMC band gaps. The DMC excitonic and quasiparticle gaps for monolayer GeSe in the table are fully extrapolated results (see Fig. 6), as are the corresponding bulk values. In Table V, all DFT calculations yield a smaller indirect band gap than direct gaps, suggesting the characteristics of an indirect semiconductor. While PBE, LDA, and SCAN largely underestimate band gaps compared to corresponding DMC band gaps, the hybrid functionals (PBE0, B3LYP, and HSE06) that incorporate some exact Hartree-Fock exchange yield band gaps closer to those of DMC (although still significantly smaller), highlighting the importance of including some level of electron-electron interactions beyond local and semilocal exchange and correlations and the importance of reduced electron self-interaction.

Monolayer GeSe has substantially larger band gaps, in the range of 3.2–3.6 eV, than bulk GeSe, 1.6–2 eV. This suggests that monolayer GeSe is a highly tunable wide-band-gap semiconductor using strain to manipulate the band gap and its optical absorption edge. Based on the DMC gaps, we cannot conclusively state whether the monolayer is a direct or indirect band-gap semiconductor. However, the closeness of the direct gap at the  $\Gamma$  point and the indirect gap ( $X$  to  $Y$  gap) and the strain sensitivity of the electronic structure

suggests that monolayer GeSe has a tunable direct-to-indirect gap transition.

The estimated DMC band gaps for monolayer are significantly larger than DFT band gaps. Because experimental values for the monolayer band gaps are not known and some previous DMC studies yielded overestimated band gaps compared to experimental values [43,51], we need to eliminate potential methodological errors in the estimated DMC band gaps for monolayer GeSe. (Note that the DMC bulk direct gap at the  $\Gamma$  point of 1.6 eV is close to the experimental value of 1.53 eV, which suggests that this DMC gap is not plagued by methodological errors.) A potential source of error is the fixed-node approximation: if the nodal structures for the ground-state and excited-state trial wave functions are poor, this can give rise to errors in estimated band gaps. In particular, it has been claimed that fixed-node errors in the excited state is a potential source of errors [51]. In order to eliminate such an error, we compare the DMC band gap to band gaps obtained using sCI through CIPSI in order to investigate the dependence of the band gap on the number of determinants in the wave function. Table VI shows calculated CIPSI energies for the ground and excited state in a  $1 \times 1$  GeSe monolayer cell. We computed variational energies  $E_{\text{var}}$  and second-order perturbative corrections  $E_{\text{PT}2}$  up to a maximum number of determinant ( $N_{\text{det}}$ ) of 9 264 974 for double-zeta (DZ) and 10 197 480 for triple-zeta (TZ) basis sets in order to estimate the extrapolated energy  $E_{\text{extrap}}$  for the full variational space using linear extrapolation to the limit  $E_{\text{PT}2} \rightarrow 0$ . Using

TABLE V. Calculated DFT and DMC band gaps for monolayer GeSe (in eV). Note that all band gaps are computed in the same optimized DMC geometry.

	Direct ( $\Gamma$ ) gap (eV)	Direct gap ( $X$ - $\Gamma$ )	Indirect gap	Quasiparticle gap
LDA	1.50	1.24	1.02	–
PBE	1.64	1.34	1.16	–
SCAN	1.90	1.61	1.38	–
PBE0	2.97	2.45	2.27	–
B3LYP	2.71	2.36	2.21	–
HSE06	2.29	1.87	1.67	–
DMC (bulk)	1.62(16)	–	–	1.95(21)
DMC (monolayer)	3.2(1)	3.6(2)	3.2(2)	3.1(2)



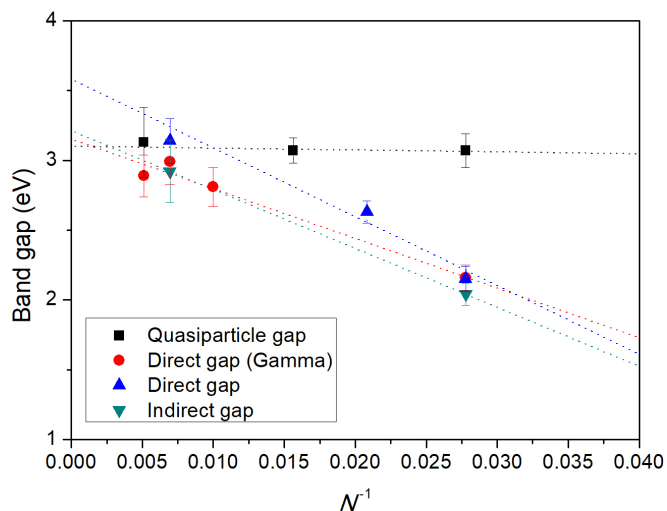


FIG. 6. DMC quasiparticle and excitonic gaps for monolayer GeSe as function of  $N^{-1}$ , where  $N$  represents the total number of atoms in the supercell. The dotted line indicates a simple linear regression fit.

$E_{\text{extrap.}}$  for DZ and TZ basis sets, we finally obtained energies extrapolated to the complete basis set (CBS) limit for the ground and for excited state with an electron promoted at the  $\Gamma$  point. The excitonic gap, which is calculated as the energy difference of  $E_{\text{extrap.}}$  in the CBS limit between the ground and excited states, is computed as 1.52 eV. Based on the good agreement of the estimated excitonic gap between CIPSI (1.52 eV) and DMC (1.36(6) eV) at the same size of supercell, we expect that the error induced by the fixed-node approximation is negligible in the DMC excitonic gap for GeSe monolayer. We were not able to compute CIPSI energies in larger supercell sizes, but the almost identical CIPSI and DMC band gaps lead us to expect that CIPSI band gaps fully extrapolated to the thermodynamic limit would exhibit band gaps very similar to the DMC band gap energy estimated using a single-determinant wave function. From these CIPSI and DMC results, we conclusively confirm that monolayer GeSe is a wide-gap semiconductor at low temperatures and

TABLE VI. Calculated CIPSI total energies in DZ and TZ quality basis sets and their extrapolated energies to the complete basis set limit.  $N_{\text{det}}$ ,  $E_{\text{var}}$ ,  $E_{\text{PT2}}$ , and  $E_{\text{extrap.}}$  represent the total number of determinants, variational energy, second-order perturbative correction, and extrapolated energy to the  $E_{\text{PT2}} = 0$  limit, respectively. Energies are given in electronvolts.

Basis	$N_{\text{det}}$	State	$E_{\text{var}}$	$E_{\text{PT2}}$	$E_{\text{extrap.}}$
DZ	9264974	Ground	-705.72	-0.97	-706.89
		Excited	-703.09	-0.94	-704.27
		Gap			2.62
TZ	10197480	Ground	-713.82	-1.76	-715.98
		Excited	-711.71	-1.81	-714.13
		Gap			1.85
CBS extrap.		Ground			-719.81
		Excited			-718.28
		Gap			1.52

that its band gap is severely underestimated by common DFT approximations.

#### IV. CONCLUSIONS

We obtained structural properties and band gaps of bulk and monolayer GeSe using QMC methods. We have shown that QMC yields accurate structural and optical properties for bulk GeSe but that DFT results vary significantly depending on the choice of XC functionals. This is analogous to the findings of Wines *et al.* [22], who showed that structural and electronic properties of monolayer GaSe obtained using DFT methods are unreliable, and even many-body perturbation theory methods such as the Bethe-Salpeter equation underestimate the direct gap. We used DMC to optimize the monolayer GeSe structure using an algorithm based on a surrogate Hessian-based method that considerably accelerated the optimization process. We found that monolayer GeSe exhibits a shallow potential energy surface minimum over a large range of lattice parameters. This makes the structures obtained by DFT very sensitive to the XC functional used.

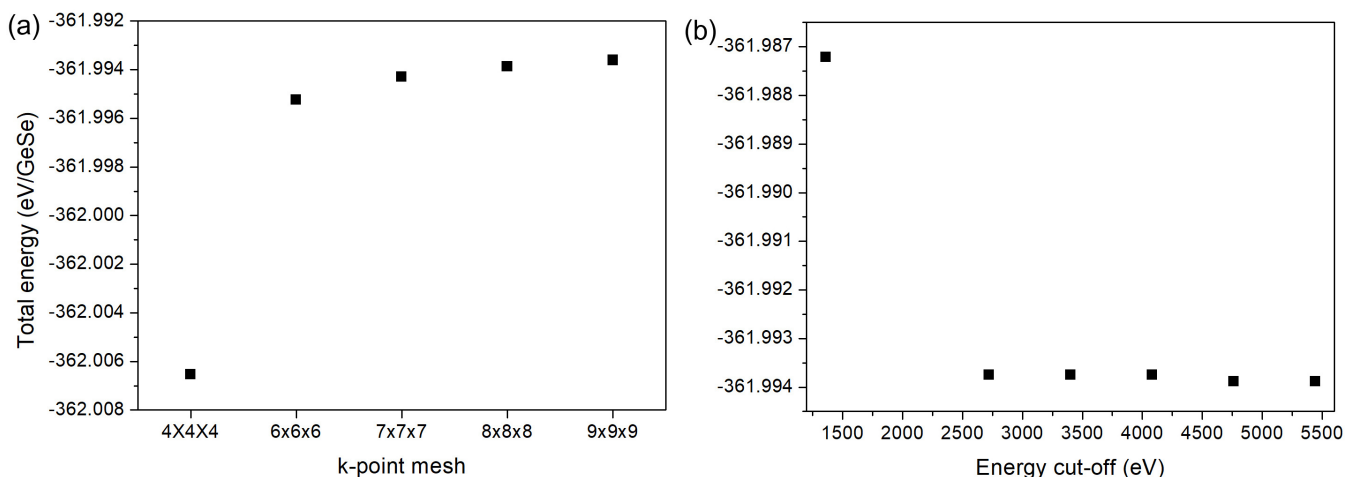


FIG. 7. PBE total energy per formula unit GeSe for bulk GeSe as a function of  $k$ -point mesh (left panel) and as a function of kinetic energy cutoff (right panel).

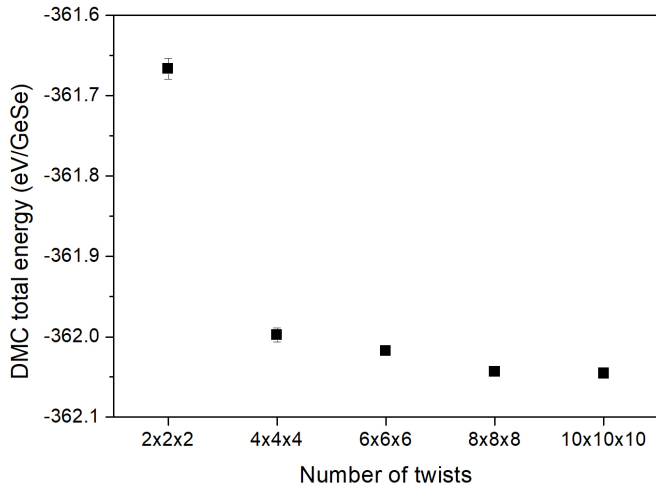


FIG. 8. DMC total energy per GeSe formula unit for bulk GeSe as function of number of twists in TABC.

Moreover, the electronic structure, including positions of band minima and band gaps, is sensitive to the structural geometry with a consequence that the DFT electronic properties also vary significantly with the choice of XC functional. We also

used DMC to estimate direct gaps at the high-symmetry  $\Gamma$  point and at a point on the high-symmetry line connecting the  $X$  and  $\Gamma$  points; we also estimated the indirect gap at a transition (from near the  $X$  point to near the  $Y$  point in the Brillouin zone) suggested by the PBE band structure based on the DMC structure. We also confirmed, using multideterminant wave functions, that the nodal error in the computed DMC gaps is small. DMC shows that the  $\Gamma$ -point direct gap is approximately the same as the indirect gap. This, and the sensitivity of the electronic structure to the physical structure, suggests that monolayer GeSe gaps are highly tunable and that a transition can be induced from a direct-gap to an indirect-gap semiconductor, with potential applications exploiting the resulting changes in optical absorption. Moreover, our work, as well as that of Wines *et al.* [22] clearly demonstrates the need for highly accurate structural and electronic structure methods in order to reliably assess the properties of GeSe and GaSe, and presumably also for most monochalcogenides as well as for transition-metal dichalcogenides, which is necessary in order to fully exploit the properties of these materials in future applications.

Input and output data from the computations [52] are available at the Materials Data Facility [53,54].

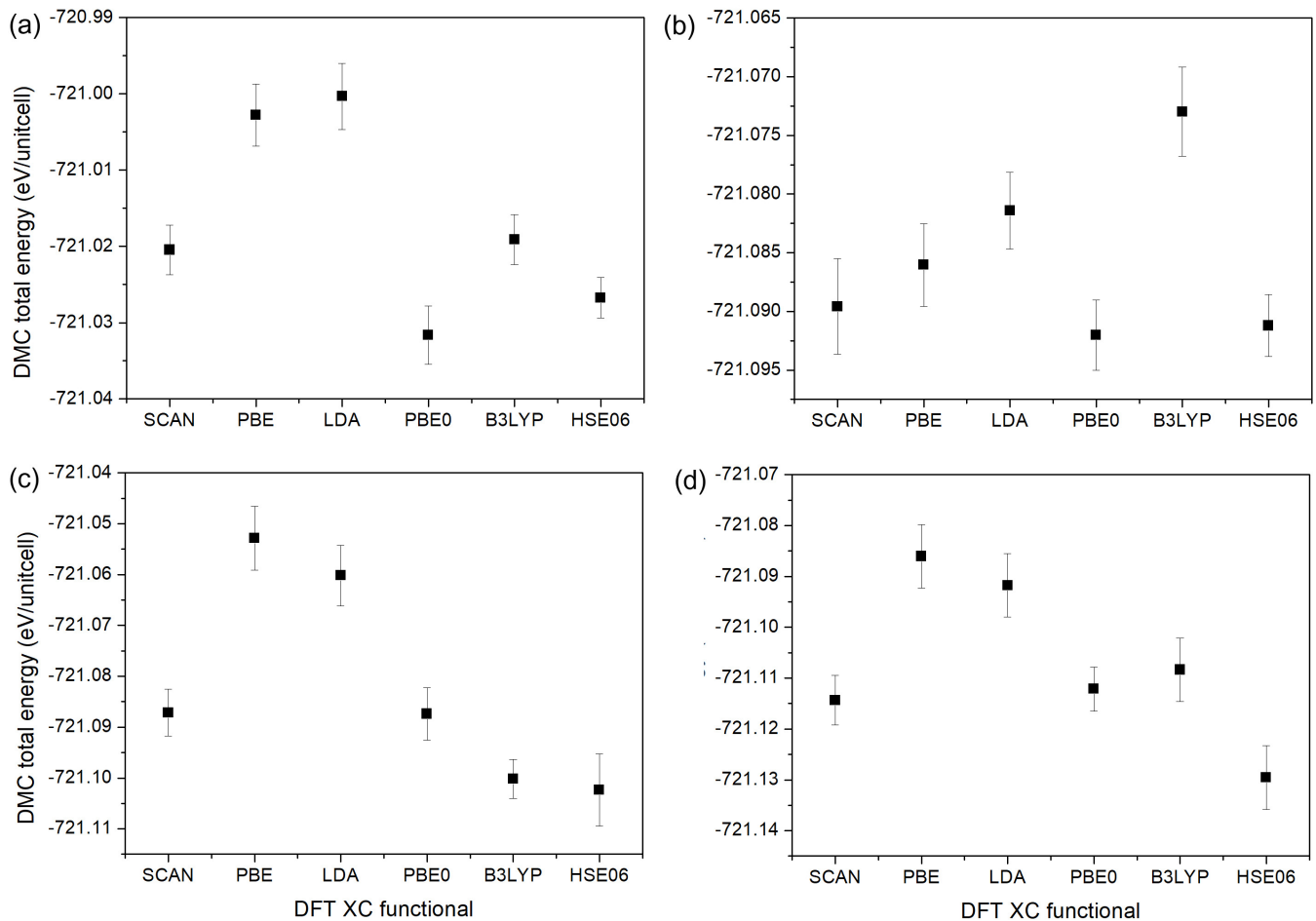


FIG. 9. DMC total energy for GeSe monolayer in lattice parameter (a)  $a = 4.05$ , (b)  $4.15$ , (c)  $4.26$ , and (d)  $4.47$  Å as a function of DFT XC functional used for atomic coordinates relaxation. Note that lattice parameter  $b$  is the same as  $3.95$  Å.

## ACKNOWLEDGMENTS

This work was supported by the US Department of Energy, Office of Science, Basic Energy Sciences, Materials Sciences and Engineering Division, as part of the Computational Materials Sciences Program and Center for Predictive Simulation of Functional Materials. An award of computer time was provided by the Innovative and Novel Computational Impact on Theory and Experiment (INCITE) program. This research used resources of the Argonne Leadership Computing Facility, which is a DOE Office of Science User Facility supported under Contract No. DE-AC02-06CH11357, and resources of the Oak Ridge Leadership Computing Facility, which is a DOE Office of Science User Facility supported under Contract No. DE-AC05-00OR22725.

APPENDIX A: CONVERGENCE WITH RESPECT TO  $k$ -POINT MESH AND TABC

Figure 7 shows the DFT PBE total energy per GeSe formula unit for bulk GeSe with respect to  $k$ -point mesh (left panel) and kinetic energy cutoff (right panel). Based on these data, we used an  $8 \times 8 \times 8$   $k$ -point mesh and a kinetic energy cutoff of 4762 eV (350 Ry). Figure 8 shows the DMC total energy per GeSe formula unit as a function of the number of twists used in TABC. The figure shows that the DMC TABC is well converged at  $8 \times 8 \times 8$  (512) twists, with only about a 2(5) meV/GeSe difference in total energy from using  $10 \times 10 \times 10$  twists. Based on the well-converged results at 512 twists for a 4-f.u. supercell, we used 64 twists for a 32-f.u. supercell, which was the smallest supercell used in our study.

## APPENDIX B: DMC CALCULATION ON RELAXED DFT GeSe ATOMIC COORDINATES

We computed DMC total energy for the monolayer with the relaxed atomic coordinates using different DFT XC functionals in order to find the best XC functional that can minimize DMC total energy at given lattice parameter. DMC was performed in large 72-f.u. supercell consisting of total

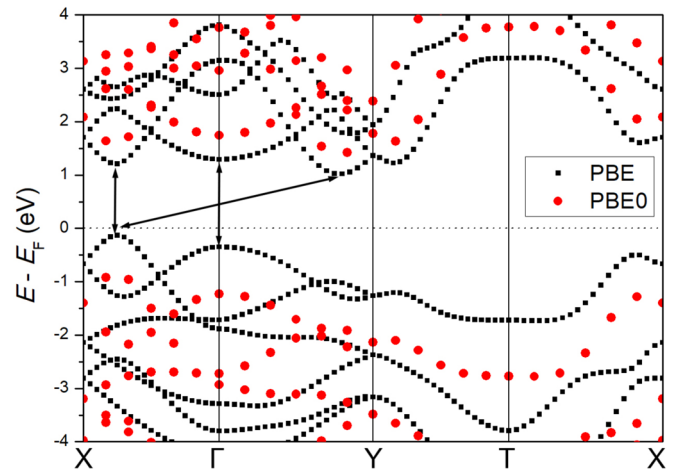


FIG. 10. DFT band structure using the PBE (black) and PBE0 (red) XC functionals. While the gap is different from that of PBE, as expected, and the direct and indirect gaps occur at the same  $k$  points as for PBE, indicated by the arrows.

720 electrons. Figure 9 represents DMC total energies in the selected lattice parameters. Because of atomic coordinates difference, we see large discrepancy in DMC energy between different XC functionals used for the structure relaxation. Between these XC functionals, we can see that HSE06 relaxed atomic coordinates show uniformly lower DMC total energy than the other XC functionals for various lattice parameters. From these results, we predict that the HSE06 XC functional can provide relatively stable GeSe atomic coordinates as compared to the other XC functionals, which lead us to decide to use the HSE06 XC functional for the geometry optimization.

## APPENDIX C: PBE0 BAND STRUCTURE

We calculated the DFT band structure for monolayer GeSe using the PBE0 XC functional on a  $12 \times 12$   $k$ -point mesh to confirm that (at least for the PBE and PBE0 functionals) the direct and indirect gaps occur at the same  $k$  points (Fig. 10).

- [1] W. Albers, C. Hass, H. J. Vink, and J. D. Wasscher, *J. Appl. Phys.* **32**, 2220 (1961).
- [2] T. Grandke and L. Ley, *Phys. Rev. B* **16**, 832 (1977).
- [3] I. Lefebvre, M. A. Szymanski, J. Olivier-Fourcade, and J. C. Jumas, *Phys. Rev. B* **58**, 1896 (1998).
- [4] V. R. Katti, P. A. Govindacharyulu, and D. N. Bose, *Thin Solid Films* **14**, 143 (1972).
- [5] A. M. Elkorashy, *Phys. Status Solidi B* **135**, 707 (1986).
- [6] A. M. Elkorashy, *Phys. Status Solidi B* **152**, 249 (1989).
- [7] D. D. Vaughn II, R. J. Patel, M. A. Hickner, and R. E. Schaak, *J. Am. Chem. Soc.* **132**, 15170 (2010).
- [8] D. D. Vaughn II, D. Sun, S. M. Levin, A. J. Biacchi, T. S. Mayer, and R. E. Schaak, *Chem. Mater.* **24**, 3643 (2012).
- [9] S.-C. Liu, Y. Mi, D.-J. Xue, Y.-X. Chen, C. He, X. Liu, J.-S. Hu, and L.-J. Wan, *Adv. Electron. Mater.* **3**, 1700141 (2017).
- [10] Y. Kim and I.-H. Choi, *J. Korean Phys. Soc.* **72**, 238 (2018).
- [11] R. Eymard and A. Otto, *Phys. Rev. B* **16**, 1616 (1977).
- [12] P. Mishra, H. Lahani, A. K. Kundu, R. Patel, G. K. Solanki, K. S. R. Menon, and B. R. Sekhar, *Semicond. Sci. Technol.* **30**, 075001 (2015).
- [13] P. A. E. Murgatroyd, M. J. Smiles, C. N. Savory, T. P. Shalvey, J. E. N. Swallow, N. Fleck, C. M. Robertson, F. Jäckel, J. Alaria, J. D. Major, D. O. Scanlon, and T. D. Veal, *Chem. Mater.* **32**, 3245 (2020).
- [14] Y. Hu, S. Zhang, S. Sun, M. Xie, B. Cai, and H. Zeng, *Appl. Phys. Lett.* **107**, 122107 (2015).
- [15] A. K. Singh and R. G. Hennig, *Appl. Phys. Lett.* **105**, 042103 (2014).
- [16] C. Xia, J. Du, W. Xiong, Y. Jia, Z. Wei, and J. Li, *J. Mater. Chem.* **5**, 13400 (2017).

- [17] T. Wang, Q. Zhang, J. Li, and C. Xia, *J. Phys. D: Appl. Phys.* **52**, 455103 (2019).
- [18] H. Shin, S. Kang, J. Koo, H. Lee, J. Kim, and Y. Kwon, *J. Chem. Phys.* **140**, 114702 (2014).
- [19] L. Shulenburg, A. D. Baczewski, Z. Zhu, J. Guan, and D. Tománek, *Nano Lett.* **15**, 8170 (2015).
- [20] H. Shin, J. Kim, H. Lee, O. Heinonen, A. Benali, and Y. Kwon, *J. Chem. Theory Comput.* **13**, 5639 (2017).
- [21] J. Ahn, I. Hong, Y. Kwon, R. C. Clay, L. Shulenburg, H. Shin, and A. Benali, *Phys. Rev. B* **98**, 085429 (2018).
- [22] D. Wines, K. Saritas, and C. Ataca, *J. Chem. Phys.* **153**, 154704 (2020).
- [23] P. J. Reynolds, D. M. Ceperley, B. J. Alder, and W. A. Lester, *J. Chem. Phys.* **77**, 5593 (1982).
- [24] W. M. C. Foulkes, L. Mitás, R. J. Needs, and G. Rajagopal, *Rev. Mod. Phys.* **73**, 33 (2001).
- [25] J. Kim, A. Baczewski, T. Beaudet, A. Benali, C. Bennett, M. Berrill, N. Blunt, E. J. L. Borda, M. Casula, D. Ceperley, S. Chiesa, B. K. Clark, R. Clay, K. Delaney, M. Dewing, K. Esler, H. Hao, O. Heinonen, P. R. C. Kent, J. T. Krogel, M. G. Lopez, Y. Luo, F. Malone, R. Martin, A. Mathuriya, J. McMinis, C. Melton, L. Mitás, M. A. Morales, E. Neuscamm, W. Parker, S. Flores, N. A. Romero, B. Rubenstein, J. Shea, H. Shin, L. Shulenburg, A. Tillack, J. Townsend, N. Tubman, B. van der Goetz, J. Vincent, D. C. Yang, Y. Yang, S. Zhang, L. Zhao *et al.*, *J. Phys.: Condens. Matter* **30**, 195901 (2018).
- [26] P. R. C. Kent, A. Annaberdiev, A. Benali, M. C. Bennett, E. J. Landinez Borda, P. Doak, H. Hao, K. D. Jordan, J. T. Krogel, I. Kylänpää, J. Lee, Y. Luo, F. D. Malone, C. A. Melton, L. Mitás, M. A. Morales, E. Neuscamm, F. A. Reboredo, B. Rubenstein, K. Saritas *et al.*, *J. Chem. Phys.* **152**, 174105 (2020).
- [27] P. Giannozzi, S. Baroni, N. Bonini, M. Calandra, R. Car, C. Cavazzoni, D. Ceresoli, G. L. Chiarotti, M. Cococcioni, I. Dabo, A. D. Corso, S. de Gironcoli *et al.*, *J. Phys.: Condens. Matter* **21**, 395502 (2009).
- [28] J. P. Perdew, K. Burke, and M. Ernzerhof, *Phys. Rev. Lett.* **77**, 3865 (1996).
- [29] M. Burkatzki, C. Filippi, and M. Dolg, *J. Chem. Phys.* **126**, 234105 (2007).
- [30] M. Burkatzki, C. Filippi, and M. Dolg, *J. Chem. Phys.* **129**, 164115 (2008).
- [31] C. Lin, F. H. Zong, and D. M. Ceperley, *Phys. Rev. E* **64**, 016702 (2001).
- [32] B. Huron, J. P. Malrieu, and P. Rancurel, *J. Chem. Phys.* **58**, 5745 (1973).
- [33] Y. Garniron, T. Applencourt, K. Gasperich, A. Benali, A. Ferté, J. Paquier, B. Pradines, R. Assaraf, P. Reinhardt, J. Toulouse, P. Barbaresco, N. Renon, G. David, J.-P. Malrieu, M. Véril, M. Caffarel, P.-F. Loos, E. Giner, and A. Scemama, *J. Chem. Theory Comput.* **15**, 3591 (2019).
- [34] Q. Sun, T. C. Berkelbach, N. S. Blunt, G. H. Booth, S. Guo, Z. Li, J. Liu, J. D. McClain, E. R. Sayfutyarova, S. Sharma, S. Wouters, and G. K. Chan, *WIREs Comput. Molec. Sci.* **8**, e1340 (2018).
- [35] G. Wang, A. Annaberdiev, C. A. Melton, M. C. Bennett, L. Shulenburg, and L. Mitás, *J. Chem. Phys.* **151**, 144110 (2019).
- [36] A. D. Becke, *J. Chem. Phys.* **98**, 5648 (1993).
- [37] C. Lee, W. Yang, and R. G. Parr, *Phys. Rev. B* **37**, 785 (1988).
- [38] S. H. Vosko, L. Wilk, and M. Nusair, *Can. J. Phys.* **58**, 1200 (1980).
- [39] P. J. Stephens, F. J. Devlin, C. F. Chabalowski, and M. J. Frisch, *J. Phys. Chem.* **98**, 11623 (1994).
- [40] R. W. G. Wyckoff, *Crystal Structures*, 2nd ed. (Interscience Publishers, New York, 2005).
- [41] J. A. Schiller, L. K. Wagner, and E. Ertekin, *Phys. Rev. B* **92**, 235209 (2015).
- [42] J. A. Santana, J. T. Krogel, P. R. C. Kent, and F. A. Reboredo, *J. Chem. Phys.* **144**, 174707 (2016).
- [43] H. Shin, Y. Luo, P. Ganesh, J. Balachandran, J. T. Krogel, P. R. C. Kent, A. Benali, and O. Heinonen, *Phys. Rev. Mater.* **1**, 073603 (2017).
- [44] H. Shin, A. Benali, Y. Luo, E. Crabb, A. Lopez-Bezanilla, L. E. Ratcliff, A. M. Jokisaari, and O. Heinonen, *Phys. Rev. Mater.* **2**, 075001 (2018).
- [45] E. P. O. O'Reilly, *J. Phys. C Solid State Phys.* **15**, 1449 (1982).
- [46] H. C. Hsueh and J. Crain, *Phys. Status Solidi B* **211**, 365 (1999).
- [47] S. Sorella and L. Capriotti, *J. Chem. Phys.* **133**, 234111 (2010).
- [48] S. Moroni, S. Saccani, and C. Filippi, *J. Chem. Theory Comput.* **10**, 4823 (2014).
- [49] H. B. Schlegel, *J. Comput. Chem.* **3**, 214 (1982).
- [50] R. Archibald, J. T. Krogel, and P. R. C. Kent, *J. Chem. Phys.* **149**, 164116 (2018).
- [51] R. J. Hunt, B. Monserrat, V. Zólyomi, and N. D. Drummond, *Phys. Rev. B* **101**, 205115 (2020).
- [52] <https://doi.org/10.18126/012d-tv94>.
- [53] B. Blaiszik, K. Chard, J. Pruyne, R. Ananthakrishnan, S. Tuecke, and I. Foster, *JOM* **68**, 2045 (2016).
- [54] B. Blaiszik, L. Ward, M. Schwarting, J. Gaff, R. Chard, D. Pike, K. Chard, and I. Foster, *MRS Communications* **9**, 1125 (2019).